Thermal analysis and high heat flux testing of unidirectional carbon-carbon composite for infrared imaging diagnostic

Mauro DALLA PALMA[1], Davide GAULE[2], Antonio PIMAZZONI[1], Roberto PASQUALOTTO[1], Gianluigi SERIANNI[1], Bernd BÖSWIRTH[3], Henri GREUNER[3]

[1]Consorzio RFX - CNR, 4 corso Stati Uniti Padova, Italy

[2]Università degli Studi di Padova, 1848 via 8 Febbraio Padova, Italy

[3]IPP Max-Planck-Institut für Plasmaphysik, 2 Boltzmannstraße Garching, Germany

Abstract

Unidirectional carbon fiber-carbon matrix (CFC) composite tiles, which are proposed to be employed in thermal imaging diagnostic of powerful particle beams, have been designed, manufactured, and tested. The particle beam is intercepted by the tiles, which erodes the carbon surface producing debris, while a plasma forms in front of the tiles due to beam-gas interaction. Carbon fibers are aligned along the tile thickness in order to transfer the heat flux from the front to the rear surface with limited thermal pattern broadening thanks to the ten times higher thermal conductivity along the fibers. This feature of the tiles allows to detect thermal radiation at the tile rear surface by thermographic cameras, producing thermograms to be correlated to energy, intensity profile, and duration of the particle beam. Thermal patterns with spatial resolution of a few mm, time resolution up to 40 ms, and maximum temperature of 1300 °C have been measured on CFC tiles exposed to accelerated hydrogen beam pulses with power densities up to 13 MW m^{-2} in the high heat flux test facility GLADIS.

Multiphysics transient non-linear parametric finite element models have been developed to simulate thermal transfer inside tiles, thermal patterns at surfaces, and thermal deformations of tiles by varying spatial distribution and peak value of the power density. Temperature gradients, hoop deformations around the heated region, location of failure region, and failure time have been analysed and discussed to recognise the tile behaviour during the high heat flux tests. Simulation models have been validated by comparing outputs to experimental measurements. Finally, model geometry and parameters have been changed to simulate the behaviour of the complete diagnostic to be used in the Source for the Production of Ions of Deuterium Extracted from a Radio frequency plasma (SPIDER) test bed of the ITER Neutral Beam Test Facility with expected power density up to 20 MW m^{-2}.

1 Introduction

Beam diagnostic calorimetry with high resolution is currently developed and tested for characterisation of energetic particle beams produced in the Source for the Production of Ions of Deuterium Extracted from a Radio frequency plasma (SPIDER) test bed of the ITER Neutral Beam Test Facility under construction at Consorzio RFX, Padova [1, 2]. The basic diagnostic concept is a calorimeter made of tiles fully intercepting the particle beam; such tiles are observed at the rear side by infrared (IR) cameras. So the idea is to use a suitable material to transfer heat from front side to rear side of the tiles. This combination of calorimetry with IR imaging demonstrated to be a diagnostic method capable of investigating properties of particle beams [3, 4]. Typical infrared images have 640 x 480 pixels corresponding to a spatial resolution of a few mm on the tile surface, 50 frames per second acquisition, 2% accuracy of the readings with temperatures above 100 °C, and maximum temperature of tile below 2000 °C in vacuum to avoid degradation of material properties. Even if SPIDER will run with pulsed operation and nominal pulse duration up to 1 hour at maximum power, particle beams with reduced power and shorter duration will be produced during first operations to optimise the particle beam parameters [5].

When a high energy beam impacts on a beam interception device like the calorimeter tiles, beam particles interact with the material surface and with the background gas. This interaction at the tiles forms a plasma placed between the observed surface and the IR thermographic camera thus disturbing the observation by altering thermograms. Another source of uncertainty is the debris emitted by the tile irradiated surface. Temperature, spatial pattern, and time behaviour of the recorded IR thermograms will be correlated to the power density distribution of the particle beam, including position, shape, and divergence. The diagnostic system, named Short-Time Retractable Instrumented Kalorimeter Experiment (STRIKE), placed in the SPIDER test bed, is shown in Fig. 1; in particular, beam divergence can be estimated by comparing thermal data of beam interception at different distances from the accelerator [6, 7].

A unidirectional fiber-reinforced composite made of carbon fiber-carbon matrix (CFC), named also carbon-carbon composite, has been developed to attain very high anisotropy for thermal conductivities in order to limit thermal pattern broadening: considering a reference system on each calorimeter tile with z axis of the beam aligned along the tile thickness and the x-y plane parallel to the front and rear surfaces (with x horizontal axis and y vertical axis), the thermal conductivity along the tile thickness shall be around 20 times larger than the in-plane thermal conductivities ($k_x = k_y \sim k_z/20$).

Carbon fiber bundles are laid down, aligned to each other, in blocks with uniform distribution of fiber bundles since identical values of thermal conductivity are desired along any direction perpendicular to the fiber in order to preserve shape of thermal patterns during transfer from front to rear tile surface, thus avoiding any spurious ovaling of thermal patterns.

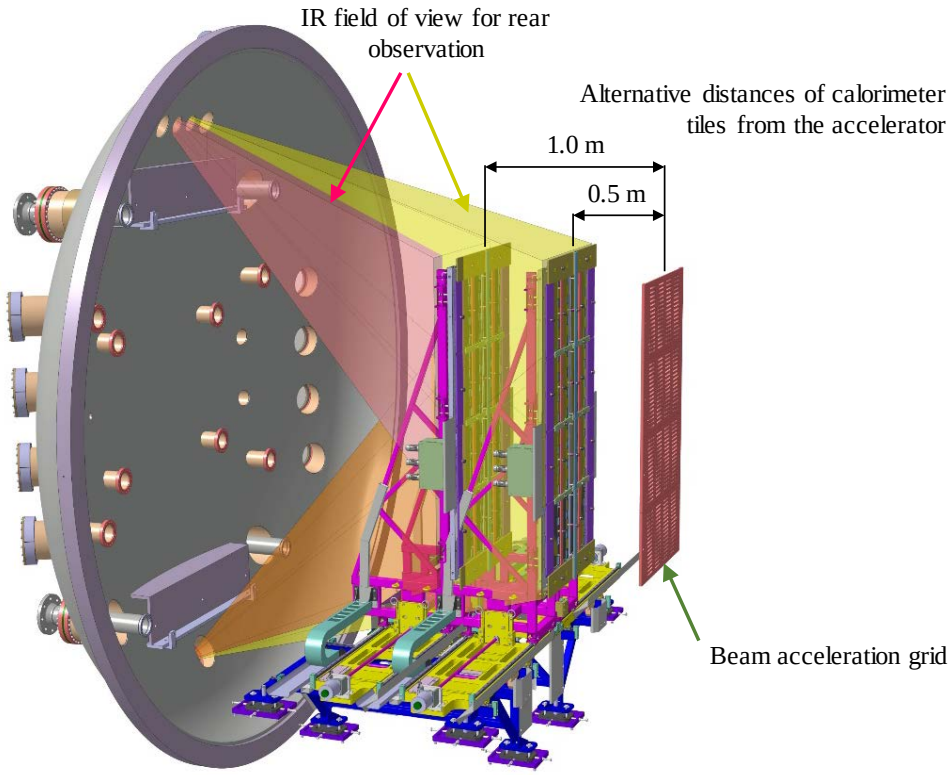

Fig. 1 - STRIKE diagnostic with calorimeter intercepting the particle beam exiting from the acceleration grid and with rear observation by IR thermographic cameras.

Different material suppliers have been involved in the project of the STRIKE diagnostic to develop the unidirectional CFC composite; then the tile prototypes had been tested [5].

Thermal properties of the CFC selected for the STRIKE diagnostic, named CX-1001U, were provided by the material manufacturer [8]. This unidirectional composite shows high non-linear temperature-dependent material properties that play significant roles in thermal behaviour within the range 20-1400 °C: the specific heat (c_p), 0.7 J kg^{-1}°C^{-1} at room temperature, has a change of 2.5 times ($c_{p|1400°C} \sim 2.5 \cdot c_{p|20\ °C}$); directional thermal conductivities (k), 30/740 W m^{-1}°C^{-1} at room temperature, have a change of 0.4 times ($k_{|1400°C} \sim 0.4 \cdot k_{|20\ °C}$); directional coefficients of thermal expansion (CTE), 9E-6 °C^{-1} at room temperature, have a change of 1.3 times ($CTE_{|1400°C} \sim 1.3 \cdot CTE_{|20\ °C}$) [8]. These strong variations must be considered when carrying out thermal analyses by implementing suitable non-linear models. In the following sections, thermal analyses and testing in the GLADIS facility are presented wherein prediction of performance by finite element (FE) models is validated by experimental campaigns.

2 Test tiles and testing facility

Tile prototypes with dimensions 188 x 142 x 20 mm^3, identified as tiles C1 and C2, have been tested in the hydrogen beam test facility GLADIS [9]. The power density profile of the beam is Gaussian-like distribution as described by Eq. 1 with peak value up to 50 MW m^{-2}.

$$p(u,v) = p_{\max} \cdot \exp\left(-\frac{u^2+v^2}{2\cdot\sigma^2}\right), \sigma = \frac{HWHM}{\sqrt{2\cdot\ln 2}}, HWHM \approx 75-90mm \qquad \text{Eq. 1}$$

where p is the power density, σ is the standard deviation of the p profile approximated by an axisymmetric Gaussian distribution and it can be derived from the half width at half maximum (*HWHM*), u and v as the horizontal and vertical coordinates respectively on the tile surface with origin of the reference system placed at the centre of the axisymmetric Gaussian distribution. The characteristic values of *HWHM* were available as a function of the peak power: *HWHM*=90mm with p_{max} = 5 MW m^{-2} and *HWHM* = 77 mm with p_{max} in the range 8-13 MW m^{-2} [9].

The tile front side intercepts only part (~100 kW) of the total particle beam power (~250 kW), so a beam dump located downstream intercepts the remaining beam power. Free thermal expansion of the material is allowed by mounting the tile on a custom stainless steel support that is thermally protected from beam interaction by graphite shields, which also slightly cover the edges of the tiles. A beam scraper is installed to realise and investigate severe temperature gradients on the tile surface up to p_{max} in a few millimetres. A stainless steel mirror on the rear side of the tile can be rotated and fastened in position to reflect the radiation to the side IR camera (Fig. 2); such an IR camera was installed at the vessel side to observe both the tile front and the tile rear.

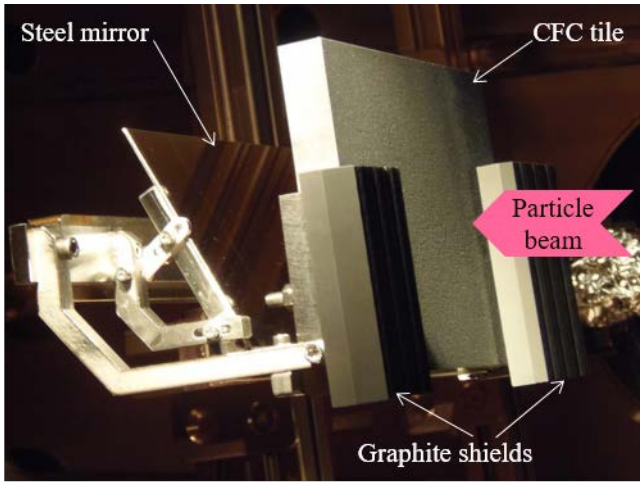

Fig. 2 - Positioning and supporting system of the CFC tile integrated with the mirror reflecting the rear side of the tile to the side IR camera.

Several tiles and different heat load configurations have been tested in GLADIS by varying three parameters viz: (1) maximum power density (p_{max}=5-13 MW m^{-2}), (2) position of the tile with respect to the beam, and (3) pulse duration (τ = 2-5 s). Among all the conditions, the three most significant for the purpose of this study are analysed and discussed in the following: tile C1 exposed to maximum power density of 10/13 MW m^{-2} and with p_{max} location x_{max} = 81 mm from the left edge and y_{max} = 52 mm from the bottom edge; tile C2 exposed to p_{max} = 8 MW m^{-2} and with x_{max} = 41 mm from the left edge and y_{max} = 52 mm from the bottom edge. An energy density parameter (e_{max}) has been calculated by multiplying p_{max} by the pulse duration in order to compute the energy deposited on tiles.

Two cameras are installed to frontally observe the tile, one IR thermographic (mounted on the testing facility and so identified as IR-GLADIS or IR front) and one visible light camera. Another IR camera, model FLIR SC655 (mounted only for these measurements and so named IR-RFX or IR rear) was installed at the vessel side. The accuracy specification of the readings is 2% for the IR-RFX camera thermal camera with temperatures above 100 °C as in this test. Beam screening carried out by the scraper and graphite shields can be identified in thermograms as shown in Fig. 3.

The analysis of thermogram data reveals the formation and propagation of cracks through the thickness of some tiles in the conditions described in section 4.

Tab. 1 – A few of different heat load configurations tested in GLADIS for tiles C1 and C2.

Tile	Pulse	p_{max}/MW m^{-2}	x_{max}/mm	τ/s	e_{max}/MJ m^{-2}	Scraper
C1	#214569	10	81	3	30	Located at x = 130 mm
C1	#214571	13	81	3	39	Located at x = 130 mm
C2	#214624	8	41	5	40	Located at x = 90 mm

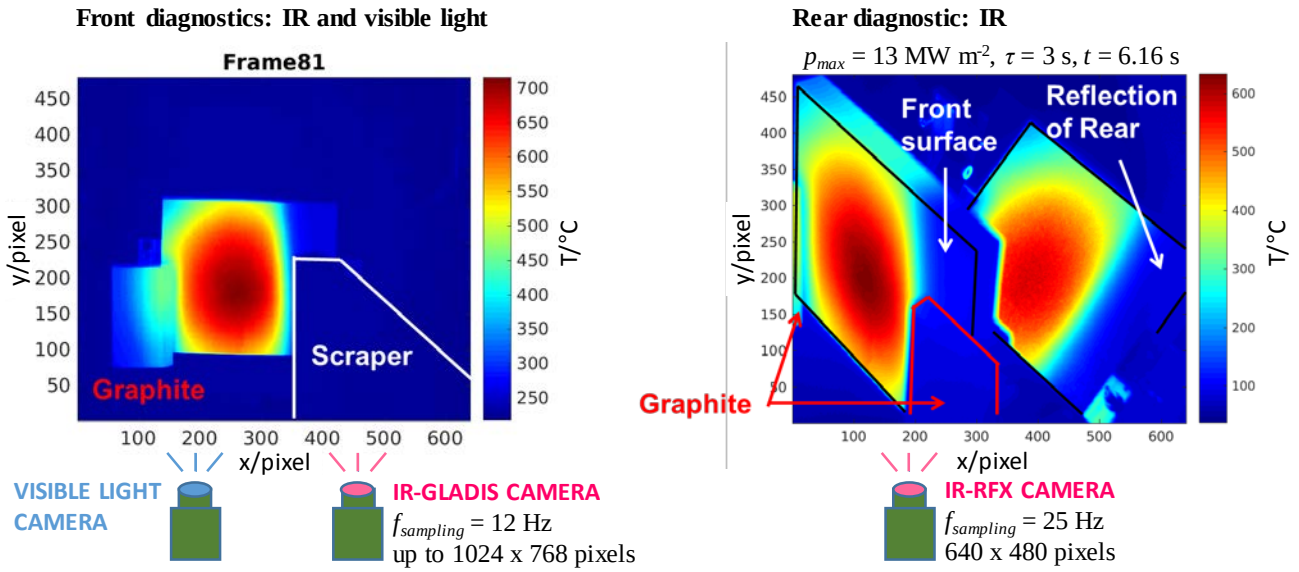

Fig. 3 – Thermograms of shot #214571 at beam OFF condition when tile C1 is already thermalized along the tile thickness (t = 6.16 s from the beginning of the beam pulse with pulse duration τ = 3 s).

3 Thermal data

Thermal data recorded from IR cameras were processed before analysis in order to implement correction of effects occurring during the measurement process: perspective, reflectivity, and transmittance. First of all, a perspective correction was applied to every image to correct the distortion due to the relative position of side camera with respect to the tile. Moreover, the temperature of the tile rear surface measured by the side IR camera (IR-RFX) was also corrected to consider the stainless steel mirror reflectivity. These corrections were applied to the entire thermograms as show in Fig. 4 where the same maximum temperature $T_{max} \approx 630$ °C was achieved at both front and rear surfaces of the thermalized tile C1 at t = 6.16 s (beam OFF condition) from the beginning of beam pulse #214571; it is worth noting that thermal data can be obtained only from portion of the thermogram due to presence of graphite shields, scraper, and tile body.

Effects of these corrections are shown in Fig. 5 for temperatures measured along the x direction at $y = y_{max}$ of thermograms detected at t = 8.0 s (beam OFF condition) of pulse #214569: after perspective transformation for rear measurement, both front and rear data have been processed considering the CFC emissivity ε = 0.85 over the total radiation spectrum [10] (blue curve "IR-front-ε=0.85" and red curve "IR-rear-ε=0.85" in Fig. 5). Rear data have been further corrected by setting the emissivity to ε = 0.75, equivalent value that includes material emissivity and mirror reflectivity in order to match the front data (overlapping of green curve "IR-rear-ε=0.75" with blue curve "IR-front-ε=0.85" in the range $50 \leq x \leq 100$ mm, Fig. 5).

Finite element (FE) parametric, non-linear, transient, thermal models have been developed to verify and investigate thermal maps on tile surfaces; temperatures calculated by simulations have been compared with experimental data as shown in Fig. 6 for temperatures at the middle horizontal axis of thermogram corresponding to t = 2 s (beam ON condition) of pulse #214569. As result of data analysis, the following considerations can be made:

- Agreement between different IR cameras is demonstrated by the left-hand side graph of Fig. 6 with overlapping of "IR-GLADIS" and "IR-RFX" camera data.
- FE simulations at rear surface (green curve "COMSOL") differ by less than 2% from IR data within the usable portion of thermogram (see the right-hand side graph of Fig. 6).
- FE simulations at front surface under-estimate temperatures measured during beam ON condition as shown by the left-hand side graph of Fig. 6. This discrepancy is ascribed to the light emitted from the plasma formed in front of

tiles and it disappears when the beam is switched off. Difficulties regarding quantification of this effect led to prefer the rear IR observation in STRIKE diagnostic.

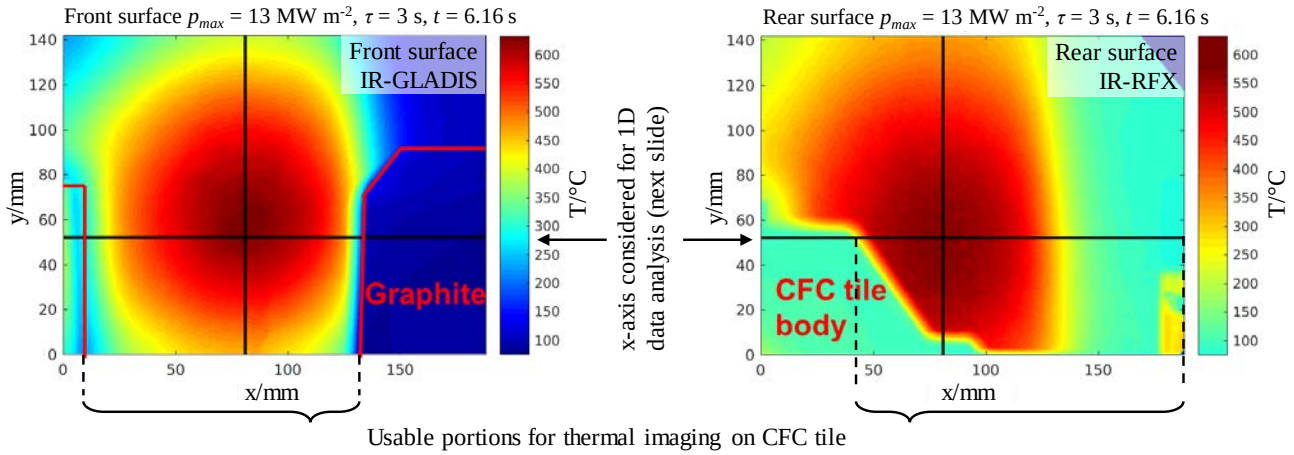

Fig. 4 - Data fitting verification at beam OFF condition of pulse #214571, thermalized tile C1 at t = 6.16 s from the beginning of the beam pulse, $T_{max} \approx 630$ °C at both front (measured with IR-GLADIS) and rear (IR-RFX) surfaces after data correction for perspective, reflectivity, and transmittance.

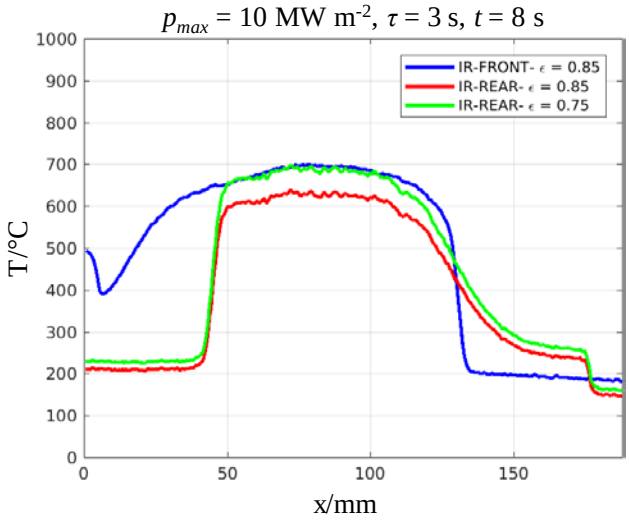

Fig. 5 – Correction of thermal data at beam OFF condition of pulse #214569, thermalized tile C1 at t = 8.0 s from the beginning of the beam pulse: both front and rear data have been corrected for glass transmittance (blue curve "IR-front-ε=0.85" and red curve "IR-rear-ε=0.85"), then rear data have been further corrected for mirror reflection (green curve "IR-rear-ε=0.75").

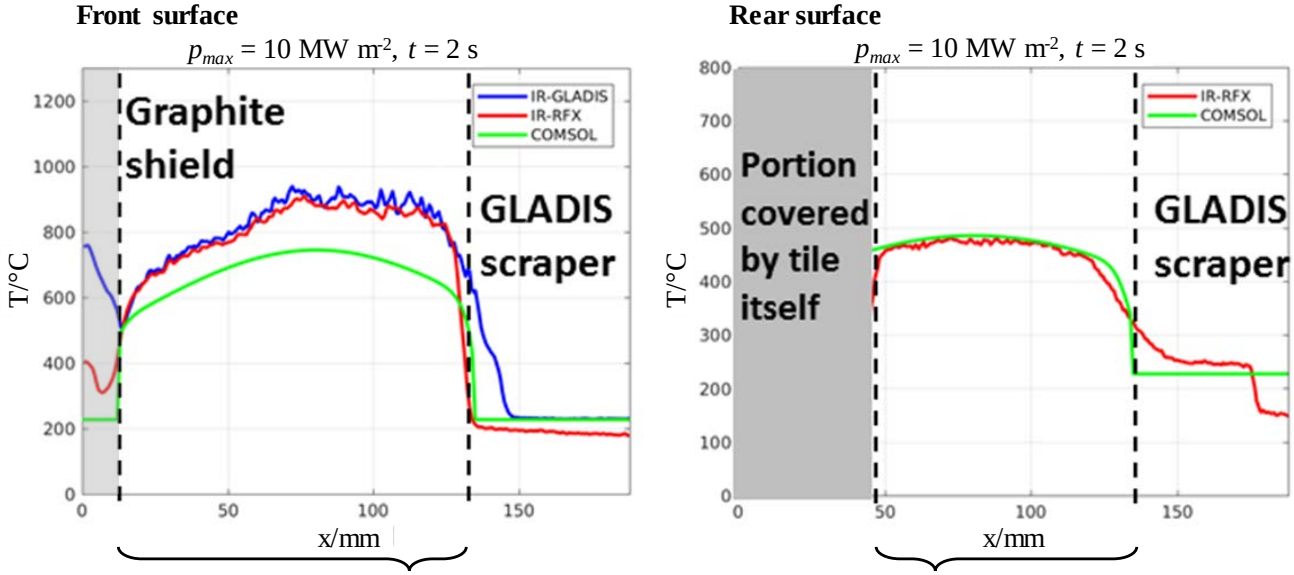

Fig. 6 - Data fitting verification at beam ON condition between simulation results and thermal data of pulse #214569, tile C1 at t = 2.0 s from the beginning of the beam pulse.

4 Observed temperature gradients

As introduced in section 2, different heat load configurations were tested also by varying the location of the thermal power: horizontal location of p_{max} is x_{max} = 81 mm for pulse #214571 (see Fig. 4) and for pulse #214569, whereas it is x_{max} = 41 mm for pulse #214624. The left-hand side of Fig. 7 shows the aiming (laser spot) indicating the position of the centre of the heat load on tile C2 before pulse #214624. The produced temperature maps are shifted towards the left when compared with those of pulse #214571 (left-hand side of Fig. 4) as shown at the right-hand side of Fig. 7; this heat load condition produces a maximum temperature of 1585 °C at the graphite shield. Tile temperatures for pulses #214569, #214571, #214624 are plotted for comparison in Fig. 8 showing thermal profiles along the x direction at $y = y_{max}$ of thermograms detected at t = 5.0 s (beam OFF condition). The maximum tile temperature T_{max} = 1304 °C is achieved with p_{max} located in the region of the tile centre and with high energy density (pulse #214571, e_{max} = 39 MJ m^{-2}, x_{max} = 81 mm). Lower tile temperatures are produced with lower energy densities: e.g. for pulse #214569, e_{max} = 30 MJ m^{-2}, x_{max} = 81 mm with maximum of T_{max} = 1184 °C. By shifting the thermal load to the left, more power is deposited on the graphite shield, so the maximum tile temperature achieved T_{max} = 1268 °C even if the energy density is the highest (pulse #214624, e_{max} = 40 MJ m^{-2}, x_{max} = 41 mm). Summarising, the presented pulses produce different temperature profiles and so diverse thermal deformation of tiles up to occurrence of failure as detailed in the following.

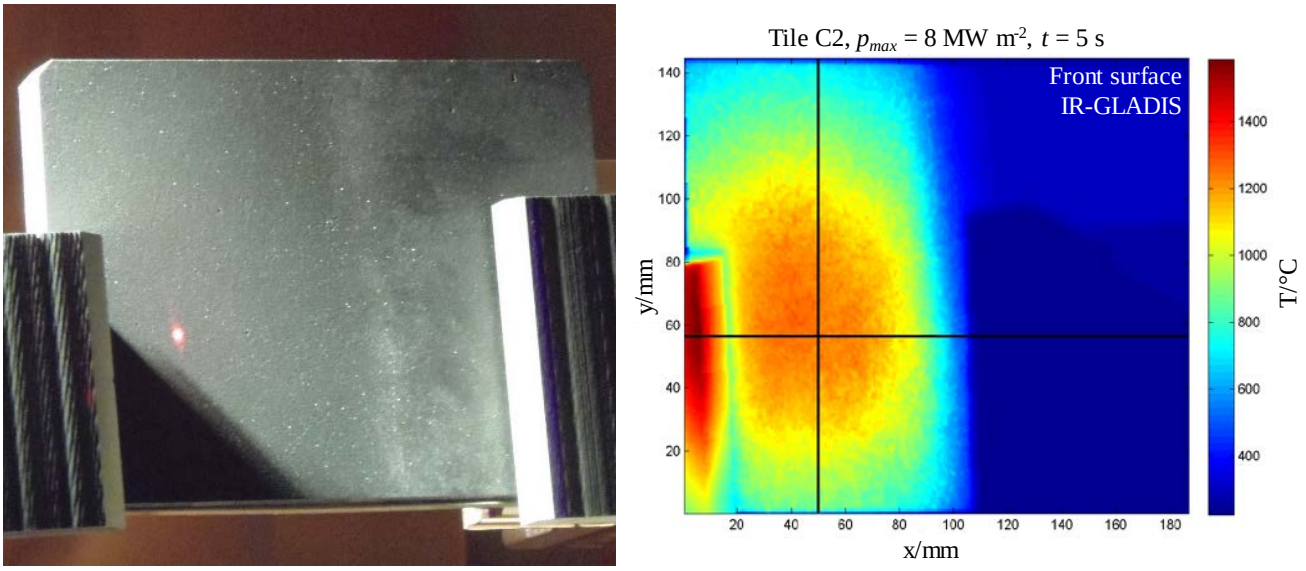

Fig. 7 – Front surface of tile C2: aiming before pulse #214624 indicating location of p_{max} (left side) and thermogram at the end of the pulse (t = 5 s).

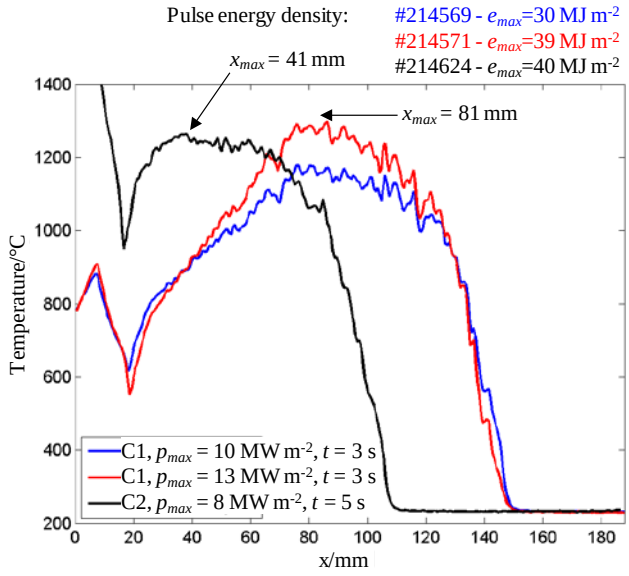

Fig. 8 - Temperatures measured along the x direction at $y = y_{max}$ of thermograms detected at t = 5.0 s (beam OFF condition) for pulses #214569, #214571, #214624; maximum energy density is indicated for comparison of peak values ($T_{max,\ \#214569}$ = 1184 °C, $T_{max,\ \#214571}$ = 1304 °C, $T_{max,\ \#214624}$ = 1268 °C).

A local discontinuity with observable temperature gradient was detected on tile C1 at the end of pulse #214569 ($x_{max,\ \#214569}$ = 81 mm, t = 3 s). This observation was attributed to a crack propagating towards the tile bottom edge; material deformations occurred in the crack region of the same tile due to thermal heating during subsequent pulses as highlighted with the blue ellipse at the right-hand side of Fig. 9 for pulse #214571. Similarly, a temperature gradient was detected on tile C2 at the end of pulse #214624 ($x_{max,\ \#214624}$ = 41 mm, t = 5 s); this gradient was attributed to a crack propagating towards the tile left edge as highlighted with the green ellipse on the left-hand side of Fig. 9. So, a change of the crack zone location was observed by varying the horizontal position of the heating load: from the bottom edge (tile C1, pulse #214569) to the left edge (tile C2, pulse #214624), where the material resistant section is minimum.

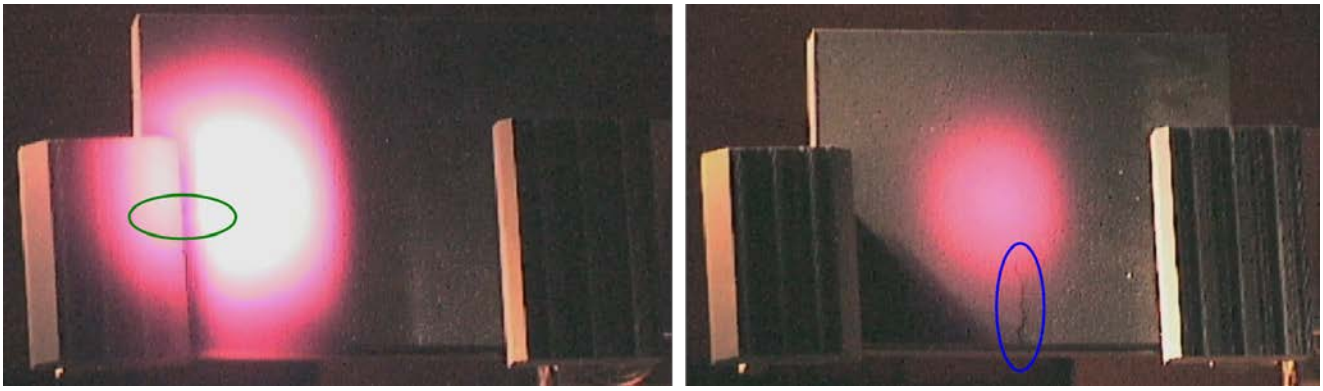

Fig. 9 – Propagated crack with temperature gradient at the left edge of tile C2 under pulse #214624 (green ellipse, left side) and at the bottom edge of tile C1 under pulse #214571 (blue ellipse, right side).

5 Analytical model

Considering the above observations, an analytical model was developed to correlate the main parameters involved in tile heating and deformation up to crack propagation by approximating the tile thermal deformation and so proposing a failure mode of thermally loaded tiles.

The thermal expansion of the heated tile core is balanced by a containment reaction developed in the peripheral cold material, so the hot core is compressed and the cold hoop is tense. The CFC is a brittle material that suffers from *tensile* stress-strain fields, especially along directions without reinforcement as occurring with hoop tensile conditions in the surrounding cold carbon matrix linking the carbon fibers. Therefore, the occurrence of failure is proposed to be predicted with a *matrix-dominated tensile failure mode* [11] for the CFC increasing its temperature and thermal expansion. Simplifying the stress-strain fields to a unidirectional condition (Kirchhoff-Love theory for thin plates with zero stresses along the thickness) [12, 13], the failure will occur when the maximum tensile stress/strain due to thermal expansion will achieve the failure limit in the carbon matrix e.g. the ultimate stress/strain (σ_u/ε_u); such a failure mode is expressed by the equations written in the system reported in Eq. 2 and is schematically represented on the right-hand side of Fig. 10.

$$\begin{cases} F_c = f \cdot (D \cdot W) = E \cdot \varepsilon_c \cdot (D \cdot W) = -E \cdot \alpha \cdot \Delta T \cdot (D \cdot W), \textit{compressed core} \\ F_h = \sigma_h \cdot (h \cdot W) \cdot (2), \textit{tense hoop} \end{cases} \qquad \text{Eq. 2}$$

where F_c in Eq. 2 is the force in the compressed core of the tile produced by the pressure f applied to the surface estimated with the diameter of the heated area (D) and by the tile depth (W), E is the in-plane elastic modulus, α is the thermal expansion coefficient, $\varepsilon_c = -\alpha \cdot \Delta T$ is the core thermal expansion corresponding to an average temperature difference ΔT between the core and the surrounding material of the tile, F_h is the reaction force in the tile tense hoop corresponding to the average stress σ_h exerted in the area given by the minimum cold resistant section $h \cdot W$. Factor 2 in the second equation is placed between brackets and neglected in the following since the analytical model has been developed to provide the correlation among the deformation parameters in the tile, not to predict expected values. As given in Eq. 3, the failure condition in the matrix will be achieved when F_h will equal the ultimate force (F_u) corresponding to $\sigma_u \approx 3$ MPa and to $\varepsilon_u \approx 0.2\%$ that are the ultimate stress and strain of the *matrix-dominated tensile failure mode* for the carbon-carbon composites [14].

$$-F_c = F_h = F_u = \sigma_u \cdot (h \cdot W) \rightarrow \sigma_u \cdot (h \cdot W) = E \cdot \alpha \cdot \Delta T \cdot (D \cdot W), \textit{ at failure} \qquad \text{Eq. 3}$$

At the end, the main parameters involved in tile deformation up to crack propagation are correlated as expressed by Eq. 4 in which the dimensionless term h/D, named *failure zone location ratio* has been isolated. The ratio h/D in Eq. 4 is function of material parameters (E, α, σ_u) and depends on ΔT: given the diameter of the heated area (D), the resistant thickness (h) increases as the temperature difference (ΔT) increases. Assuming a constant material heat capacity and a concentrated thermal load producing a severe temperature gradient, the h/D ratio increases with the heating energy. The

significance of *h/D* and the appropriateness of the *matrix-dominated tensile failure mode* for the CFC increasing its temperature due to the energy deposited by the beam will be verified in the following.

$$\frac{h}{D} \approx \frac{E \cdot \alpha}{\sigma_u} \cdot \Delta T \qquad \text{Eq. 4}$$

As explained above, compressive conditions occur in the heated region whereas a tense conditions are expected in the cold surrounding material, so the stress/strain tensor can be analysed in a local cylindrical reference system centred on the peak of the axisymmetric power density distribution heating the tile. Stresses/strains in this cylindrical reference system will be analysed along radial, hoop/circumferential, and axial directions. A qualitative distribution of hoop stresses is given on the left-hand side of Fig. 10 with *D* measured at σ_h equal to zero e.g. at the transition between compressed and tense material. The evidence of appropriateness of stress/strain component analysis in this cylindrical reference system is provided in the next section by looking at principal stress/strain directions.

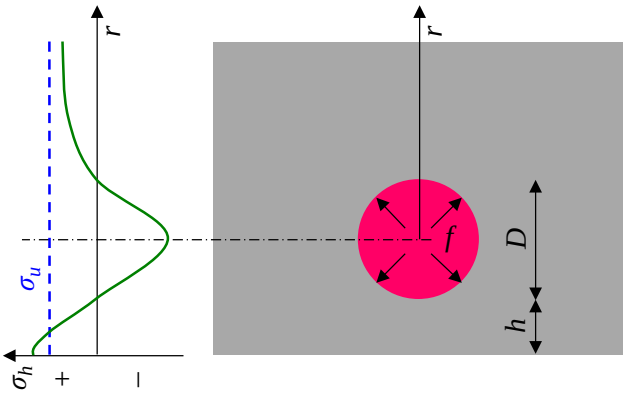

Fig. 10 – Sketch of a tile (right side) with main parameters of the model developed to propose the *matrix-dominated tensile failure mode* for the CFC tiles subjected to thermal energy: thermal pressure (*f*), diameter of the heated area (*D*), minimum resistant thickness (*h*) are shown; internal hoop stress distribution (σ_h) with example of exceeding σ_u threshold is given at the left side.

6 Finite element simulations

Multiphysics (thermal and mechanical), transient, non-linear, parametric FE models have been developed to simulate temperature profile and thermal expansion of CFC tiles subjected to thermal loads. These models were validated against experimental observations in GLADIS of temperature profiles and of crack propagations in the CFC material. Once validated, these models can be used within the validation ranges to predict temperatures and material allowable limits of CFC tiles of STRIKE operating in SPIDER.

Two commercial codes were used to simulate the behaviour of the CFC tiles: COMSOL for material temperatures and ANSYS for both material temperatures and thermal deformations. Thermal analyses using the two codes allow to verify implementation of non-linear temperature dependence of material properties within the range 20-1400 °C.

The geometric model consists of a parallelepiped with dimensions 192 x 144 x 20 mm^3 (*L* x *H* x *W*) slightly increased along the *x* and *y* directions with respect to the tile actual sizes (188 x 142 x 20 mm^3) in order to be symmetrically meshed with 4 mm surface size elements, whereas element depth is 2 mm (48 x 36 x 10 elements in total). Directional material properties have been set following the temperature dependences specified by the material supplier as introduced in section 1 [8].

The following thermal boundary conditions were applied in the FE model to simulate the in-vacuum heat transfer in a tile placed inside the GLADIS vessel: axisymmetric Gaussian *p* distribution (see Eq. 1 and left bottom corner of Fig. 2) on the front surface simulating the beam interception, adiabatic condition on all other surfaces. Thermal power radiated from the tile surfaces to the environment was neglected as it was estimated to be less than a few percent of the deposited power; this neglect is considered a conservative assumption as thermal radiation contributes to decrease the maximum material temperatures so reducing temperature gradients and correspondingly thermal deformations. Thermal power conducted by

the CFC material in contact with tile supports was neglected given the small area of the contact surfaces and the poor thermal conduction condition of the in-vacuum interface. Isostatic mechanical constraints were applied to the tile to allow for free thermal expansion of the heated material as it occurs during thermal testing in GLADIS.

The beam power with high peak density (p_{max} = 5-13 MW m^{-2}) was applied to the model as a thermal load linearly ramped in 0.1 s. Linearly ramping the power allows for minimal computed residuals and so faster convergence during application of the very high thermal load in the non-linear transient analysis. This simulation ramp time of 0.1 s is more than one order of magnitude smaller than the experimented pulse durations, thus the error in the thermal energy computation is considered negligible. Moreover, this simulation ramp time is rather larger than the typical experimental beam switch-on time (1.1 ms) of the GLADIS facility [15]. In order to achieve convergence of the transient finite element simulations and to follow temperature gradients and the tile thermal expansion, the numerical time step of 0.01 s was specified during the 0.1 s ramp, whereas 0.1 s numerical time step was set for beam-on up to 6-15 s maximum time. These specific time steps have been obtained by carrying out a sensitivity analysis and comparing results obtained from both FE codes. Analyses produce accurate temperature maps simulating the front surface heating with entire application of the thermal load and the material heat transfer with very different values of directional thermal conductivity. Thermal pattern results at tile front and rear surfaces have been compared with thermogram data producing matching of temperature patterns as shown in Fig. 6.

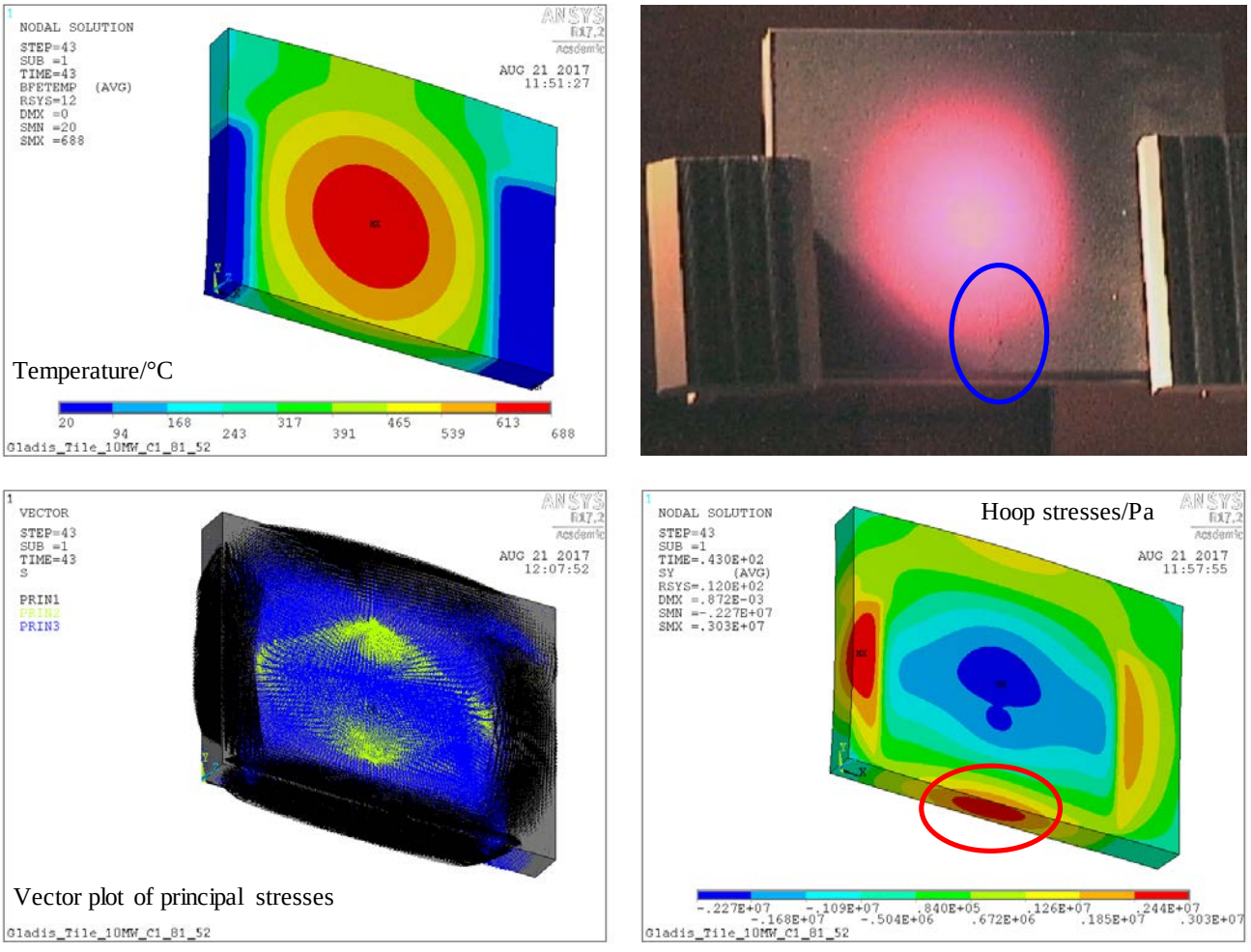

Fig. 11 – Failure condition with hoop stresses achieving 3 MPa = σ_u at t = 2.5 s for pulse #214569 with centre of axisymmetric Gaussian distribution located at x_{max} = 81 mm from the tile left edge: thermal map (top left), vector plot of principal stresses (bottom left), region of maximum hoop stresses through the entire thickness at the tile bottom edge (red oval at the bottom right), and identification of propagated crack on thermalized tile (blue oval at top right); magnification factor of deformed shape of simulated tile is 10.

Thermo-mechanical results of FE simulations were post-processed and analysed considering the *matrix-dominated tensile failure mode* for observed crack propagated on tiles; Fig. 11 summarises these analyses for tile C1 heated with pulse #214569. The distribution of the first principal stresses (*PRIN1* with black arrows at the bottom left corner of Fig. 11) corresponds to the cold tile area shown in the thermal analysis (top left corner). The direction of *PRIN1* is circumferential with respect to the heating centre and so these stresses represent the hoop component of the stress tensor in a cylindrical

reference system; hoop stresses (indicated as *SY* in the FE code instead of σ_h) are shown in the stress map at the bottom right corner of Fig. 11. The origin of such cylindrical reference system is located at the minimum value of third principal stresses (*PRIN3* with blue arrows at the bottom left corner) that corresponds to the location of the maximum tile temperature and to the position of the peak of the applied power density. Temperature, stress distribution, and the location of the failure region with *SY* = 3 MPa = σ_u achieved at t = 2.5 s are shown by contours of Fig. 11 for pulse #214569 with pulse duration τ = 3.0 s. Hoop stresses (contours at the bottom right corner) are maximum in an area extending through the entire thickness at the tile bottom edge so predicting failure occurrence in that region corresponding to experimental observation (blue oval on the thermalized tile at the top right corner).

Thermo-mechanical results of FE simulations for tile C2 heated with pulse #214624 have been post-processed and analysed as shown in Fig. 12. The distribution of the first principal stresses (*PRIN1* with black arrows at the bottom left corner of Fig. 12) corresponds to the cold tile area shown in the thermal analysis (top left corner). The direction of *PRIN1* is circumferential with respect to the heating centre and so representing the hoop component of the stress tensor in a cylindrical reference system; hoop stresses (*SY*) are shown in the stress map at the bottom right corner of Fig. 12. Temperature, stress distribution, and the location of the failure region achieved at t = 2.4 s are shown by contours of Fig. 12 for pulse #214624 with duration τ = 5.0 s. Hoop stresses (contours at the bottom right corner) are maximum in an area extending through the entire thickness at the tile left edge so predicting failure occurrence in that region corresponding to experimental observation (green oval on the thermalized tile at the top right corner).

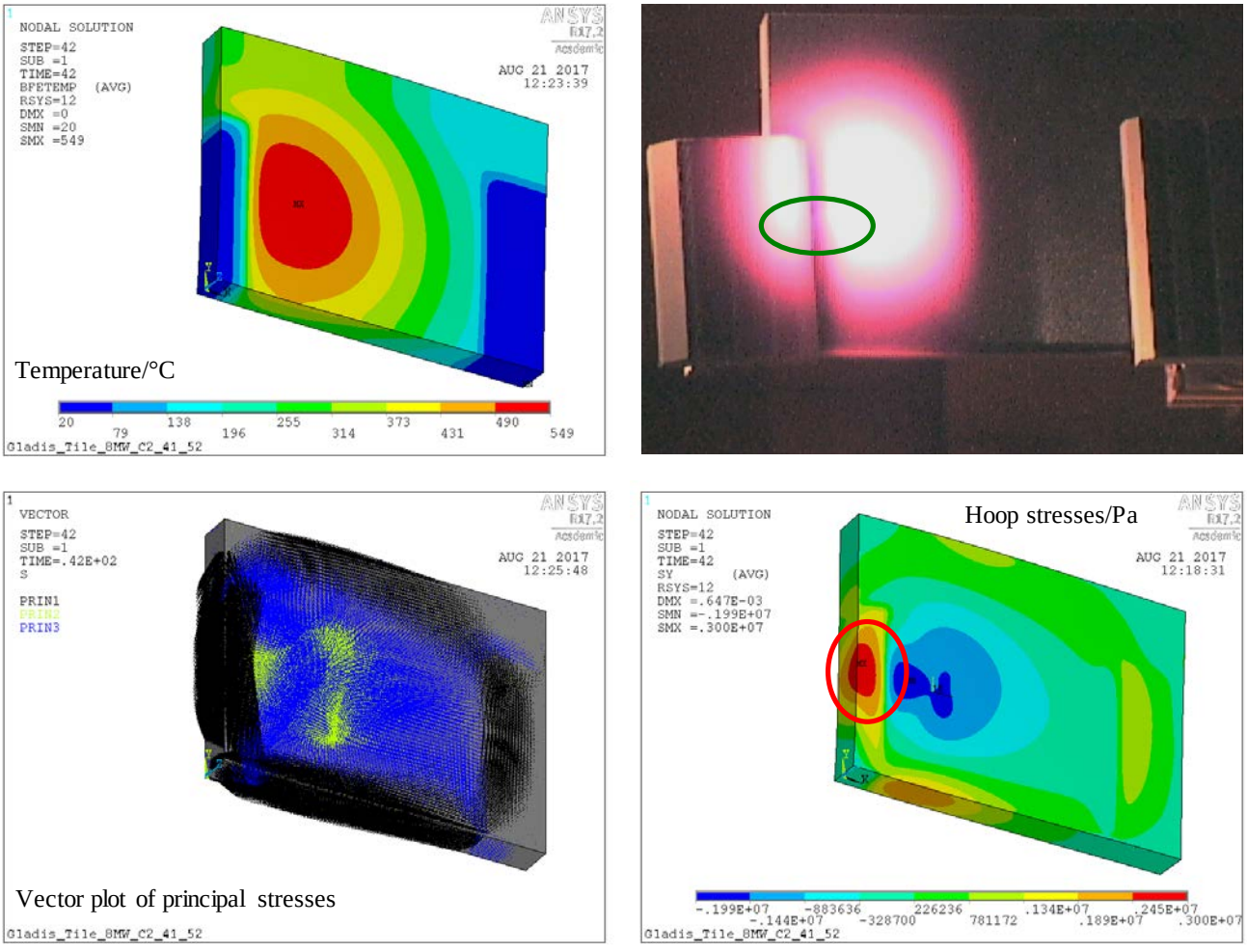

Fig. 12 – Failure condition with hoop stresses achieving 3 MPa = σ_u at t = 2.4 s for pulse #214624 with centre of axisymmetric Gaussian distribution located at x_{max} = 41 mm from the tile left edge: thermal map (top left), vector plot of principal stresses (bottom left), region of maximum hoop stresses through the entire thickness at the tile left edge (red oval at the bottom right), and identification of propagated crack on thermalized tile (green oval at the top right); magnification factor of deformed shape of simulated tile is 10.

As described above and shown in Fig. 11 and Fig. 12, the developed FE model is able to predict the location of the failure region in thermally heated tiles. The capability of the FE model acknowledges the proposed *matrix-dominated tensile failure mode* to predict conditions under which CFC tiles fail under the action of external thermal loads. Above evidences confirm that cracks propagate in the minimum resistant section experiencing tensile conditions due to the temperature gradient.

The *failure zone location ratio* has been further investigated by simulating the crack propagation condition with several peaks of the thermal load (p_{max} = 5-13 MW m^{-2}). Transient thermo-mechanical FE simulations were carried out by applying all these thermal loading conditions and results were post-processed by analysing achievement of maximum hoop stress / strain at 3 MPa / 0.2% so identifying the failure time and the location of the failure region. Detailed results are shown in Fig 13 by varying the peak of the power density (p_{max} = 5, 8, 10, 13 MW m^{-2}) and with position of p_{max} at x_{max} = 86 mm and y_{max} = 54 mm (fixed location of the external thermal load at 1/2·*L* and 3/8·*H*): temperature maps at failure are depicted at the left-hand side, hoop strains with maximum values *EPTOY* ≈ 0.2% are shown at the right-hand side of Fig. 13. The strain *EPTOY* is the total mechanical strain produced by thermal deformations that includes elastic, plastic, and creep contributions along the *Y* direction that is the hoop/circumferential component of the strain tensor in the local cylindrical reference system centred on the peak of the axisymmetric power density distribution heating the tile. Results show that the failure time increases reducing the peak of power density and that the maximum energy density is almost constant for higher power densities (p_{max} = 8, 10, 13 MW m^{-2}).

Also the location of the axisymmetric Gaussian *p* distribution has been changed to investigate the effect on the ratio *h/D* evaluated at the minimum resistant section at failure: p_{max} has been placed at four different locations on the tile along the vertical direction identified by x_{max} = 86 mm (1/2·*L*) and with y_{max} = 18 mm (1/8·*H*), 36 mm (1/4·*H*), 54 mm (3/8·*H*), 72 mm (1/2·*H*). Simulations results are represented in graph of Fig. 14 in which the ratio *h/D* is calculated from averages of both *h* and *D* for each position y_{max}.

Lines in the graph of Fig. 14 look like hyperbolas with the coordinate axes as asymptotes and with constant product $t_{failure} \cdot p_{max} = e_{failure}$ meaning that tile failure can be approximated with an energy criterion: the deposited beam energy heats the tile with temperature gradients producing thermal expansion up to crack propagation at the minimum resistant section. Solid lines in Fig. 14 are hyperbolas with distance from the origin of the reference system decreasing as *h/D* diminishes: the energy to achieve crack propagation ($e_{failure}$) decreases by moving down the p_{max} from y_{max} = 72 mm to 54 mm and so diminishing the thickness of the cold resistant section. A further shift down of *p* (y_{max} = 18/36 mm) produces a 15% loss of heating power and higher temperatures at the tile bottom edge with respect to y_{max} = 54/72 mm due to the small radial gradient of the *p*, thus requiring larger heating time and correspondingly increased temperature to achieve *SY* ≈ 3 MPa / *EPTOY* ≈ 0.2% for crack propagation; these considerations justify the location of dashed lines in Fig. 14 that are translated horizontally with increased $t_{failure}$. Experimental crack propagations observed for beam pulses with durations 3 s and 5 s are affected by some uncertainties as failures can only be detected at the end of pulses and the identification when they exactly occur is not possible. Despite this, experimental failures shown in Fig. 14 are consistent with simulation results, so the FE model has been validated and is considered capable of estimating the failure time of tiles subjected to thermal load. Indeed simplifications and hypotheses made in the model were accurately evaluated: thermal radiation from tile to environment was ignored as it is negligible, thermal conduction from the CFC material in contact with tile supports was neglected, crack propagation occurs at $\sigma_u \approx 3$ MPa or at $\varepsilon_u \approx 0.2\%$ independently from local temperature. Moreover, experimental execution of beam pulses produces progressive heating of the tile with increased initial material temperature; this pre-heating effect was not simulated and 20 °C uniform tile temperature was applied in the FE model at the beginning of each pulse.

In conclusion, analysis results with different thermal load locations were summarised by pairs p_{max}, $t_{failure}$ with location in the graph of Fig. 14 depending on the temperature gradient in the CFC material. Nevertheless a unidirectional trend of *h/D* cannot be figured out for the analysed thermal loads, the significance of the *failure zone location ratio* was demonstrated and it will be very important with highly peaked distributions of *p*. Indeed, the concentration of thermal power in a narrow area produces negligible loss of power, high intensity of the temperature gradient, and low temperature of the resistant section even if changing the position of p_{max}.

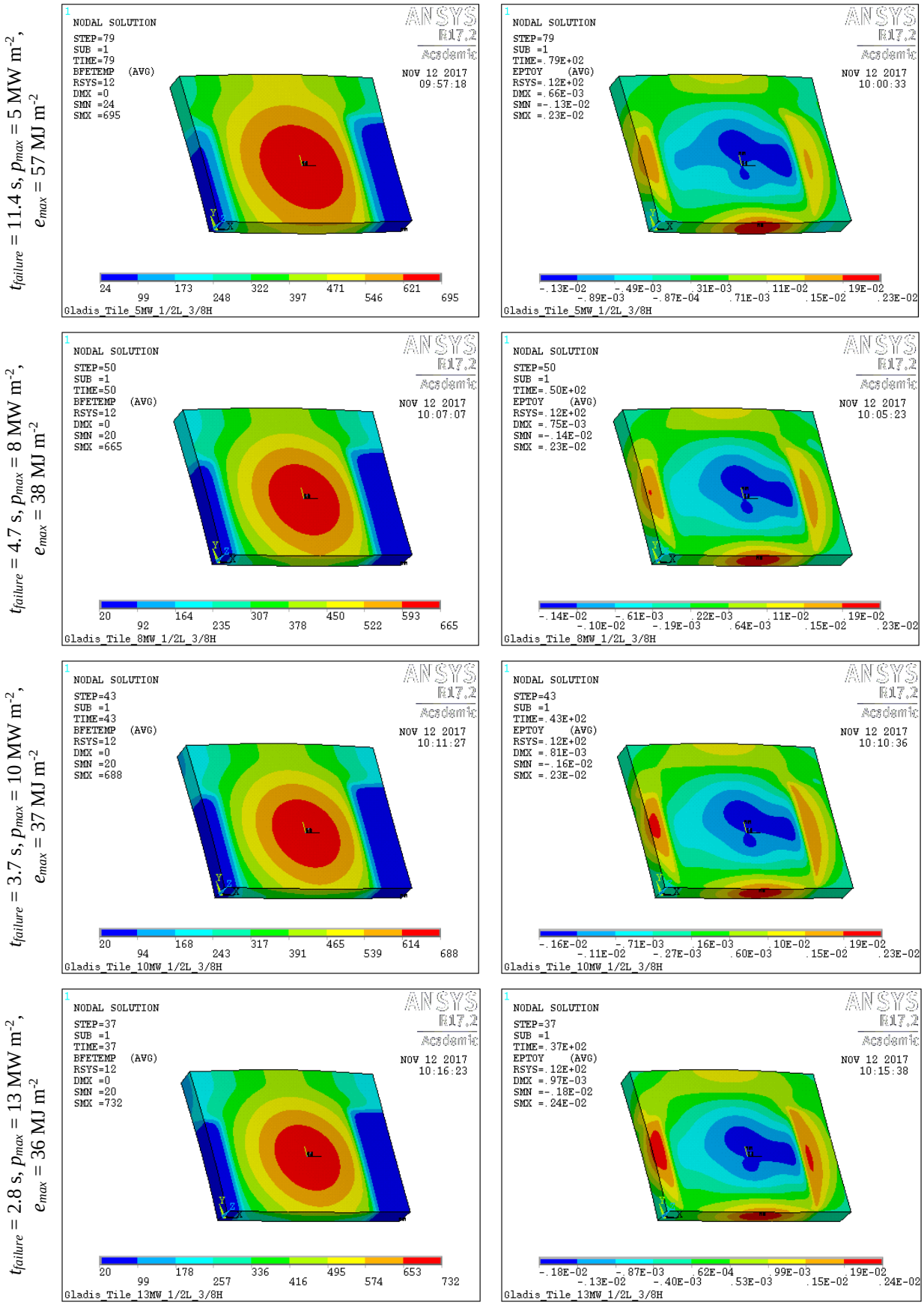

Fig. 13 – Temperature maps in °C at failure (left side) and hoop strains with maximum identifying the failure region located at the tile bottom edge (right side); values obtained with fixed location of p_{max} at 1/2·L and 3/8·H and changing the peak of power density; magnification factor of deformed shape is 10.

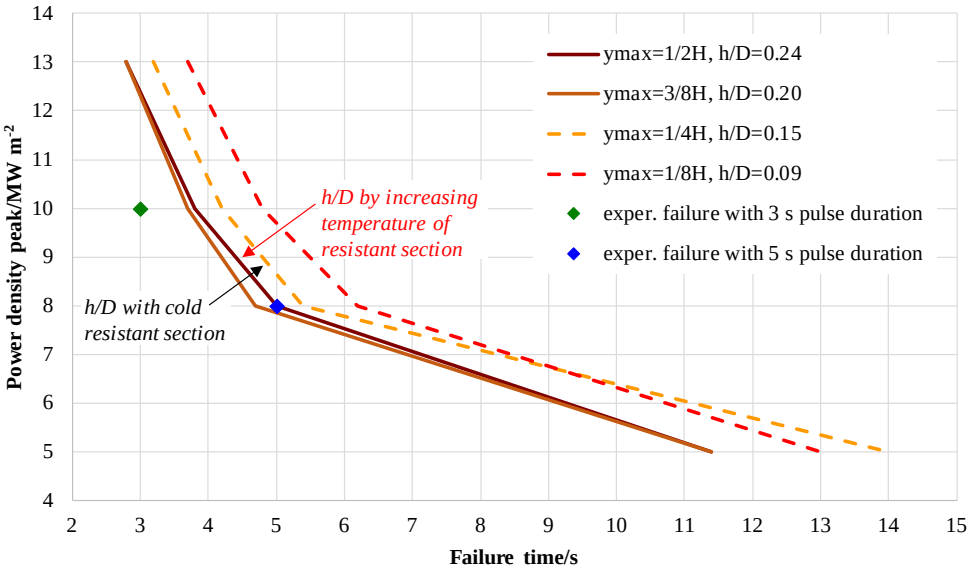

Fig. 14 – Detected experimental cracks and representation of the energy criterion for crack simulations with different peaks of the thermal load (p_{max} = 5-13 MW m^{-2}) and with application of the axisymmetric Gaussian p distribution at x_{max} = 86 mm (1/2·L) and at different locations along the vertical direction (y_{max}).

7 Conclusions

The particle beam thermal imaging diagnostic rely on unidirectional carbon fiber-carbon matrix composite (CFC) with very high ratio of thermal conductivities: the one along the thickness direction is about 20 times larger than those in the in-plane directions.

Tiles made of such material were manufactured and tested under high heat loads in the GLADIS facility. Thermal patterns were recorded using two infrared (IR) cameras supported by one visible light camera. IR data were processed, analysed, and simulated by finite element (FE) non-linear thermal models capable of replicating the measured temperatures.

Change of the crack zone position was observed by experimentally varying the location of the thermal peak load, so a *matrix-dominated tensile failure mode* based on hoop stress-strain components was proposed in order to recognize and predict the failure conditions. The crack will propagate at the minimum resistant section due to temperature gradient under application of thermal loads.

A thermo-mechanical, transient, non-linear, parametric FE model was developed to simulate temperature profile and thermal expansion of the CFC tiles subjected to thermal loads. Two loading conditions with different locations of the thermal load were analysed, matching the experimental cracks. This agreement allows to validate the model capable of predicting the position of the crack zone achieving ultimate values of tensile hoop stress/strain and adopting the proposed *matrix-dominated tensile failure mode*.

Other thermal load positions were investigated by simulating the crack propagation condition with different peaks of the thermal load (within the range 5-13 MW m^{-2}); analysis results approximate the experimental failure time and show that tile failure can be approximated with an energy criterion: failure occurs at almost constant value of the product between failure time and maximum power density.

The parametric FE model can be used within validation ranges and hypotheses to predict temperatures, location of the crack region, and failure time of tiles operating under different heating conditions; in particular, the model can simulate tiles of the STRIKE diagnostic to be used in the SPIDER Test Bed of the ITER Neutral Beam Test Facility with focussed multi-beams (80 particle beams for each tile) and expected power density up to 20 MW m^{-2}. The presented energy criterion represents a preliminary tool to predict maximum allowable pulse duration avoiding crack propagation in CFC tiles during STRIKE operation given the power density distribution of the particle beam; further investigations are ongoing to consider effects of beam divergence on temperature gradient.

Acknowledgements

The work leading to this publication has been funded partially by Fusion for Energy. This publication reflects the views only of the authors, and F4E cannot be held responsible for any use which may be made of the information contained therein. The views and opinions expressed herein do not necessarily reflect those of the ITER Organization.

References

[1] Toigo V. et al. The PRIMA Test Facility: SPIDER and MITICA test-beds for ITER neutral beam injectors. New J. Physics 2017;19:085004.

[2] Toigo V. et al. The ITER Neutral Beam Test Facility towards SPIDER operation. 2017 Nucl. Fusion 57 086027.

[3] Ciric D. et al. Beam profiles measurement using a unidirectional CFC-target and infrared imaging. Proceedings of the 18th Symposium on Fusion Technology, Karlsruhe, Germany, 22–26 August 1994.

[4] Nocentini R. et al. Advanced ion beam calorimetry for the test facility ELISE. AIP Conference Proceedings 1655, 060006 (2015); doi: 10.1063/1.4916475.

[5] De Muri M. et al. High energy flux thermo-mechanical test of 1D-carbon-carbon fibre composite prototypes for the SPIDER diagnostic calorimeter, Rev. Sci. Instrum. 2014;85(2):02A718.

[6] Serianni G. et al. Neutralisation and transport of negative ion beams: physics and diagnostics. New J. Physics 2017;19:045003.

[7] Pasqualotto R. et al. A suite of diagnostics to validate and optimize the prototype ITER neutral beam injector. J. Instrum. 2017;12:C10009.

[8] Toyo Tanso CO., LTD, CC-02037/Technical Data Sheet.

[9] Greuner H. et al. High heat flux facility GLADIS: Operational characteristics and results of W7-X pre-series target tests. J. Nucl. Mater. 2007;1444:367-4.

[10] Serianni G. et al. Test of 1D carbon-carbon composite prototype tiles for the SPIDER diagnostic calorimeter. AIP Conf. Proc. 2017;1869:060007-7.

[11] Hashin Z. Failure Criteria for Unidirectional Fiber Composites, J. Appl. Mech. 1980;47:329-6.

[12] A. E. H. Love, On the small free vibrations and deformations of elastic shells, Philosophical trans. of the Royal Society (London), 1888, Vol. série A, N° 17 p. 491–549.

[13] Reddy, J. N., 2007, Theory and analysis of elastic plates and shells, CRC Press, Taylor and Francis.

[14] Zaldivar RJ, Rellick GS. Failure Modes of Unidirectional Ultra-High-Modulus Carbon-Fiber/Carbon-Matrix Composite. The Aerospace Corporation El Segundo, CA 1998; SMC-TR-98-13; Aerospace Report No. TR-93(3935)-15.

[15] Greuner H. et al. Experimental determination of the transient heat absorption of W divertor materials. 2014 Phys. Scr. 2014 0140035.